applied sciences

MDPI

Article

Estimation via Laser Ultrasonics of the Ultrasonic Attenuation in a Polycrystalline Aluminum Thin Plate Using Complex Wavenumber Recovery in the Vicinity of a Zero-Group-Velocity Lamb Mode

Guqi Yan [1], Samuel Raetz [1,*], Jean-Philippe Groby [1], Aroune Duclos [1], Alan Geslain [2], Nikolay Chigarev [1], Vitalyi E. Gusev [1] and Vincent Tournat [1]

[1] Laboratoire d'Acoustique de l'Université du Mans (LAUM), UMR 6613, Institut d'Acoustique-Graduate School (IA-GS), CNRS, Le Mans Université, 72085 Le Mans, France; yanguqi1@gmail.com (G.Y.); jean-philippe.groby@univ-lemans.fr (J.-P.G.); aroune.duclos@univ-lemans.fr (A.D.); nikolay.chigarev@univ-lemans.fr (N.C.); vitali.goussev@univ-lemans.fr (V.E.G.); vincent.tournat@univ-lemans.fr (V.T.)

[2] DRIVE EA1859 Laboratory, Université de Bourgogne–Franche Comté, 58027 Nevers, France; alan.geslain@u-bourgogne.fr

* Correspondence: samuel.raetz@univ-lemans.fr; Tel.: +33-(0)2-43-83-36-30

Abstract: In this paper, we present a method to recover the complex wavenumber dispersion relations using spatial Laplace transform from experimental spatiotemporal signals measured by laser ultrasonic technique. The proposed method was applied on zero-group-velocity Lamb modes in order to extract the ultrasonic attenuation in a polycrystalline aluminum plate of about 70 µm thickness. The difference between the experimental and theoretical Laplace Fourier transforms was minimized in the least square sense to extract the complex amplitudes and complex wavenumbers of the modes at about 40 MHz. The experimental results were compared to values reported in the literature that were measured by other means and those estimated by using the quality factor extracted from a single temporal signal.

Keywords: laser ultrasonics; zero-group-velocity Lamb modes; complex dispersion curves; ultrasonic attenuation; non-destructive testing and evaluation

Citation: Yan, G.; Raetz, S.; Groby, J.-P.; Duclos, A.; Geslain, A.; Chigarev, N.; Gusev, V.E.; Tournat, V. Estimation via Laser Ultrasonics of the Ultrasonic Attenuation in a Polycrystalline Aluminum Thin Plate Using Complex Wavenumber Recovery in the Vicinity of a Zero-Group-Velocity Lamb Mode. *Appl. Sci.* **2021**, *11*, 6924. https://doi.org/10.3390/app11156924

Academic Editor: Vincent Laude

Received: 29 June 2021
Accepted: 22 July 2021
Published: 28 July 2021

1. Introduction

The characterization of the material microstructures has been a continuous interest of research, because of the microstructure effect on the performance and reliability of materials and manufactured components. The mechanical properties of a material, including ultrasonic attenuation, are intrinsically linked to its microstructures. Ultrasonic non-destructive techniques, among other methods, are good candidates to characterize the mechanical properties of a wide range of materials, which have resulted in numerous publications (see, e.g., the review [1] and references therein). Ultrasonic attenuation can be associated to the decrease in amplitude of the elastic waves while interacting with the microstructures and is attributed to different mechanisms. The fundamental nature of the elastic wave absorption and scattering mechanisms leading to ultrasonic attenuation has been studied for decades [2]. An extended state-of-the-art summary on this research topic is out of the scope of this paper. In the present work, the tested material is a polycrystalline aluminum plate, which is a material commonly used for manufactured components. In that case, the main source of attenuation is normally the scattering of the elastic waves by grains [3]. This is the reason characterizing the ultrasonic attenuation in a polycrystalline material allows gathering insightful information on its microstructure.

The Lamb waves are commonly used guided waves for ultrasonic non-destructive testing of plate-like structures [4–8]. In recent years, specific Lamb modes have drawn

increasing attention for their particular features: the zero-group-velocity (ZGV) Lamb modes. The ZGV Lamb modes have indeed proved to be an efficient tool for locally and precisely probing the thickness of a sample [9–13], the mechanical properties of isotropic [14–17] and anisotropic materials [18], or for detecting damage in composite [19] and metallic materials [20,21], at megahertz frequencies (even up to gigahertz [22,23] frequencies). These particular modes correspond to local resonances of the inspected structure and result from the interference of two Lamb waves having an opposite phase velocity and coalescing at a single frequency (see further discussion in the next section). The laser ultrasonics technique is an efficient technique to generate and detect such local resonances because it is contactless. The all-optical configuration, consisting of a pulsed laser source to generate elastic waves and an interferometer to probe the associated normal displacement field, avoids contact with the sample, which could widen or even suppress resonances. When the acoustic energy leakage of ZGV Lamb modes to the air is negligible and the plate surfaces are parallel, these ZGV Lamb modes generated and detected by lasers are good candidates to probe locally the ultrasonic attenuation of the plate. This idea was followed in 2008 by measuring the decay time of the first ZGV Lamb mode below 10 MHz in copper, duralumin, and steel plates [24] and, later, at higher frequencies ($\sim$2 GHz), in samples of tungsten with thicknesses in the micrometer range [25]. This decay time is closely related to the quality factor of the local ZGV resonance, the measure of which could therefore also give access to the local ultrasonic attenuation [11,15] or else to the structural adhesive bonding in multi-layer assemblies [26].

Besides the local property of the ZGV Lamb modes, another interesting feature is the complex nature of the two Lamb modes composing a ZGV Lamb mode in the vicinity of the coexistence frequency, referred to as the ZGV frequency. Below that ZGV frequency, the two Lamb modes have complex wavenumbers and are therefore evanescent. Above the ZGV frequency and in the ideal case of a non-attenuating material, these two modes have real wavenumbers and are purely propagative. In the presence of attenuation, the wavenumbers of all Lamb modes are complex, which is enhanced in the vicinity of a ZGV frequency. We propose to take advantage of this enhanced effect to measure the ultrasonic attenuation by recovering the complex dispersion curves through a single treatment of laser ultrasound B-scan data via the SLaTCoW method (spatial Laplace transform for complex wave-number recovery [27]).

The paper is organized as follows. The theoretical dispersion curves in the complex wavenumber-frequency space in aluminum plate are presented in Section 2. The experimental setup and the two-used scanning configurations are introduced in Section 3. In Section 4, the SLaTCoW method is shortly summarized and applied to reconstruct the dispersion curves in the complex wavenumber-frequency space from the experimental data. The ultrasonic attenuation of the assessed material is then estimated by minimizing the difference between the theoretical and measured complex dispersion curves. Finally, these measured values of ultrasonic attenuation are discussed, as well as the perspectives of the presented work.

2. Zero-Group-Velocity Lamb Modes in an Aluminum Plate

Generally, the propagation of Lamb waves is dispersive. Thus, many studies, both experimental and theoretical/numerical, focused on the dispersion curves of such guided waves [28–35].

The dispersion curves of the symmetric (S) Lamb modes can be plotted after numerically solving the well-known Rayleigh–Lamb equation that reads [36,37]

$$\frac{\tan(ph)}{\tan(qh)} + \frac{(q^2 - k^2)^2}{4k^2pq} = 0, \quad (1)$$

for the S modes, where h stands for half of the thickness of the plate, $p^2 = \omega^2(1/V_L^2 - 1/V^2)$, and $q^2 = \omega^2(1/V_T^2 - 1/V^2)$. In the latter expressions, ω denotes the angular frequency and V_L and V_T stand for the longitudinal and shear acoustic waves velocities of

the material, respectively. Note that $k = k_r + \imath k_i$ is the complex wavenumber with k_r and k_i the real and imaginary parts, respectively.

The dispersion curves of the S Lamb modes are plotted in Figure 1, for a 71.5 µm thick aluminum plate with elastic properties presented in Table 1 and neglecting the attenuation. The thickness is chosen to match that of the plate used in the experiments (see Section 3). In Figure 1a, the dispersion curves are plotted in the real plane k_r–f, for $k_r \geq 0$, where parts of the branches where $k_i \neq 0$ have been omitted for clarity. The complete view of the dispersion curves is plotted in three dimensions in the complex wavenumber-frequency space (k_r, k_i, f) in Figure 1b. The symmetrical modes propagating in both directions with positive (solid lines) and negative (dashed lines) group velocity, with subscript "b" for backward mode (this is the case where phase and group velocities are opposite in signs), are plotted for $(k_r, k_i) \in \mathbb{R}^2$: S_0, S_2, S_1, and S_4 modes are in solid lines, whereas S_{-0}, S_{-2}, S_{-1}, and S_{-4} are in dashed lines. The modes are here numbered according to the number of nodes present in the thickness of the plate [37]. The arrows indicate the position of the first ZGV mode, i.e., the S_1S_2-ZGV mode, on the dispersion curves. Indeed, at particular positions on the dispersion curves of the modes, the group velocity $V_g = \partial\omega/\partial k_r$ vanishes, while the phase velocity $V_{ph} = \omega/k_r$ remains finite. In the case where the dissipation due to the material or to the waveguide boundaries is neglected, it is known that there is a rigorous identity between the group velocity and the velocity of energy transport under very general conditions [38]. Therefore, for the ZGV points where the group velocity vanishes while the phase velocity remains finite, the resonances remain locally at the position of the excitation.

In Figure 1b, it is clear that a ZGV mode results from the interference of guided modes coexisting for a unique couple of frequency/wavenumber. In the specific case where the attenuation is neglected, it is seen that the four modes, S_2 and S_{-1b} as well as S_{-2} and S_{1b}, are coincident two by two at ZGV points (black points in Figure 1b). At these points, the four modes have exactly the same frequency f_{ZGV} and the same wavelength, i.e., same absolute value $|k_r^{ZGV}|$ of the real part of the wavenumber: $k_r^{ZGV} = k_{S_2}(f_{ZGV}) = -k_{S_{1b}}(f_{ZGV}) = -k_{S_{-2}}(f_{ZGV}) = k_{S_{-1b}}(f_{ZGV})$. In the case where the material presents some attenuation (always the case in reality), the four branches have non-zero positive (S_2, S_{1b}) and negative (S_{-2}, S_{-1b}) imaginary parts k_i for all k_r and f. Therefore, the branches of the modes S_2 and S_{-1b}, on the one hand, and of the modes S_{-2} and S_{1b}, on the other hand, no longer coincide at the ZGV points, which actually no longer exist. The detected resonance would then correspond to the interference of the S_2 and S_{1b} modes and/or the S_{-2} and S_{-1b} modes. The latter statement explains why the ZGV resonance is called S_1S_2. Note that the term "ZGV resonance" is used to discuss the resonance effect associated with the existence of the ZGV Lamb mode but accounting also for the frequencies close to that of the ZGV mode where the Lamb waves have non-zero but really small group velocity.

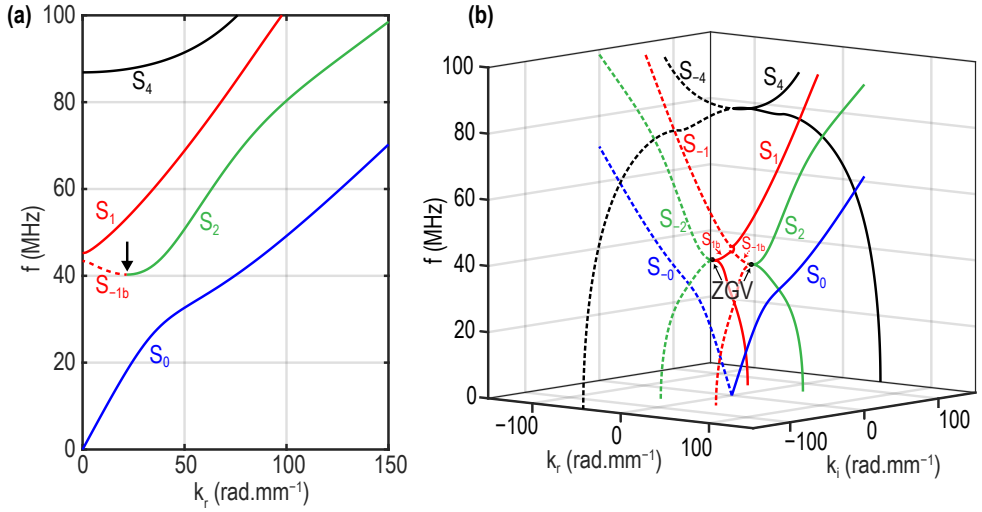

Figure 1. Dispersion curves of the S Lamb modes in a 71.5 µm thick aluminum plate: (**a**) dispersion curves in the real plane k_r-f with a black arrow indicating the position of the S_1S_2-ZGV mode; (**b**) three-dimensional view (k_r, k_i, f) of the complex dispersion curves for the first symmetrical modes propagating in both directions with positive (solid lines) and negative (dashed lines) group velocity, with subscript "b" for backward mode: S_0, S_2, S_1, and S_4 modes are plotted in solid lines and S_{-0}, S_{-2}, S_{-1}, and S_{-4} are plotted in dashed lines. The colors of S_0/S_{-0}, S_2/S_{-2}, S_1/S_{-1}, and S_4/S_{-4} modes are blue, green, red, and black, respectively. Two black solid circles show the position of the ZGV point as indicated by the black arrows labeled "ZGV".

Table 1. Elastic properties for aluminum sample.

Parameter	Value
Thickness (µm) $2h$	71.5
Density (kg/m^3) ρ	2700
Longitudinal velocity (m/s) V_L	6450
Shear velocity (m/s) V_T	3100

Although the branches of all the modes will be shifted in the positive or negative direction along the k_i-axis due to the attenuation and depending on their propagation direction, this shift will be easier to assess close to resonances than on propagative modes. Close to resonances, such as those at the ZGV points or else at $k_r = 0$ where there are the thickness mode longitudinal and shear resonances, the attenuation indeed induces a larger change on k_i than away from resonances where the group velocity is no longer negligible (note that, as discussed in [31], in the case of material absorption where the definition $V_g = \partial\omega/\partial k_r$ of the group velocity leads to abnormal velocities, a possibility is "to consider [instead] the velocity of energy transport which is defined as the ratio of energy flow to mechanical energy density"). Therefore, although propagative modes do attenuate, good precision on the estimation of this attenuation will require a longer propagation distance where the group velocity is not closer to zero than in the vicinity of a resonance. This larger effect of the attenuation on k_i close to a resonance for a given mode is associated to the path of the Lamb mode branch that goes from a propagating branch in the plane $k_i = 0$ to a non-propagating branch, i.e., out of the plane $k_i = 0$, when the frequency is below the resonance (cut-off or ZGV) frequency (Figure 1b). For further details on the path of Lamb mode branches in absorbing plates, the readers are referred to the work of Simonetti and Lowe [31]. We propose in the following to take advantage of this larger effect of attenuation on k_i in the vicinity of a ZGV resonance to estimate the attenuation.

From the calculations of the dispersion curves in the case of the 71.5 µm thick aluminum plate free of attenuation shown in Figure 1, it is expected to experimentally detect a ZGV resonance associated to the S_1S_2-ZGV mode with frequency $f_{S_1S_2} = 40.28$ MHz and wavenumber $k_{S_1S_2} = 21.93$ rad.mm^{-1}. The recovery of the complex wavenumber later on is therefore performed around those frequency and wavenumber.

3. Experimental Setup and Measurements

The experimental setup used in this work is schematically illustrated in Figure 2a. The pump laser (pulse duration close to 0.75 ns with a repetition rate of 1 kHz) had an optical wavelength of 1064 nm and was focused into a stretched ellipse close to a line generation source: the minor axis of the ellipse is ∼20 µm along the x-axis and its major axis is ∼500 µm along the y-axis. The z-axis, as depicted in Figure 2b,c, is normal to the free surfaces of the plate, its origin being in the middle of the plate thickness. Another continuous laser (with a wavelength of 532 nm) was focused to a circular spot (diameter ∼20 µm) in the vicinity of the line source and was used for ultrasonic wave detection thanks to the beam deflection technique. Note that this technique is often used for laser ultrasound probe [39–44]. The calibration of the coincidence of the generation line source and the detection circular spot was controlled by a rotational mirror. The aluminum plate was attached on a three-dimensional stage. With this experimental setup, two different scans were conducted: (1) to characterize the sample thickness, the rotational mirror position was fixed, the distance between the position of the pump laser and that of the probe laser was fixed at $d = 20$ µm, and the sample was moved along the x-axis (see Figure 2b); (2) to perform spatiotemporal measurements (B-scan), the sample position was fixed and the mirror rotated in order to move the generation from the position x = 0 mm, where generation and detection are superimposed, to the position $x = L$, with a scanning step of $d = 20$ µm (see Figure 2c). Note that, in Configuration (1), as shown in Figure 2b, the distance d between the pump and the probe was mandatory for the detection of the ZGV resonance since the beam-deflection technique is sensitive to the radial gradient of the normal displacement (which is zero at x = 0, i.e., $\partial u_z^{\mathrm{ZGV}}(x = 0)/\partial x = 0$, where u_z^{ZGV} stands for the part of the normal displacement that is due to the ZGV resonance). Before the B-scan measurements, the sample was polished to improve the reflection of the probe beam, but the sample thickness was thus changed. If the thickness varies along the measured area, this may result in enhancing the probed attenuation due to thickness inhomogeneity. This unsought effect should be reduced in order to measure the ultrasonic attenuation associated mainly to material properties. To do so, a characterization of the thickness was therefore performed to find a location of a constant thickness of the plate. The experimental characterization of the thickness changes of the plate was carried out by looking at the changes of the ZGV frequency along the x-axis: all other parameters being unchanged, the relative variation of the thickness is equal to the opposite of the relative variation of the ZGV resonance frequency [12]. It seems important to underline here that the polishing of the sample, which can modify the film thickness homogeneity, is generally not mandatory at all in laser ultrasonics. We did so because of the detection technique we used. However, commercially available interferometers could indeed allow optical detection of the laser-generated elastic waves on rough surfaces.

In Figure 3a, a typical signal measured when the generation and detection are at a distance of d = 20 µm is shown. The low frequency part of the signal corresponds to the first anti-symmetric mode A_0, which is dominant. By zooming in on the time signal (inset), we can see a higher frequency oscillation, which corresponds to the ZGV resonance. When this signal is Fourier transformed (see Figure 3b), a resonance with quality factor of $Q_{Al} = 61$ (full width at half maximum) shows up around 40 MHz. The quality factor of the local ZGV resonance in an aluminum plate can be used for estimating the local attenuation using the method proposed by C. Prada et al. [24], which can further be compared with the attenuation as recovered by the SLaTCoW method (for further discussions, see Section 4). By scanning the aluminum plate over 30 mm in front of the

fixed laser beams (Configuration (1), Figure 2b), a zone of constant thickness of 4 mm-long in aluminum is found. At this location, the thickness is estimated to be $2h = 71.5$ µm, which is obtained thanks to the measure of the ZGV resonance frequency and assuming the elastic properties of our aluminum sample to be those reported in Table 1. Note that, starting from a nominal thickness of 75 µm, the polishing leads to a varying thickness over the complete 30 mm long scanned line in the range [70.7 µm, 74.5 µm], which was estimated with the variation of the ZGV frequency. Spatiotemporal measurements were then carried out using the scanning configuration shown in Figure 2c. We note here that Figure 3c shows the normalized signal amplitude as a function of x (distance between the generation and the detection areas) on the horizontal axis and of time on the vertical axis. Furthermore, in Figure 3c, the A_0 Lamb mode is mainly observed, i.e., the low frequency content. From these measurements, a double Fourier transform,

$$\widetilde{u}(k_r, \omega) = \int_0^T \int_0^L u(x,t) e^{-\imath k_r x} e^{\imath \omega t} \mathrm{d}x \mathrm{d}t, \tag{2}$$

is applied in order to see the wavenumber-frequency diagram in the real plane (k_r, f) shown in Figure 3d, with T the maximum time of acquisition and L the length of the scanned line. In the zoomed part around the ZGV frequency (Figure 3e), three branches are present (from left to right): mode S_{1b}, mode S_2, and mode A_1 (second anti-symmetric mode). Note that, since the measurements are made in a single direction, i.e., in the direction of the positive group velocities, the branch of the S_{1b} mode appears where the real part of the wavenumber is negative and that of the S_{-1b} mode is not present since its group velocity is negative. Following this first analysis of the experimental results in the real plane, it is now proposed to use the SLaTCoW method [27], based on the spatial Laplace transform for the recovery of the experimental dispersion curves in the complex wavenumber-frequency space.

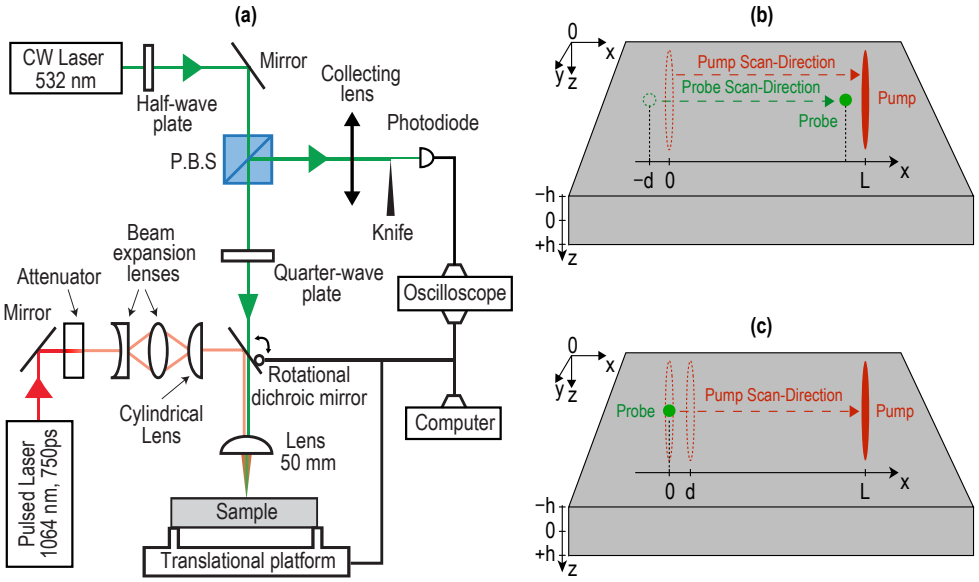

Figure 2. (**a**) Experimental setup. (**b**,**c**) Illustration of the two scanning configurations used: (**b**) the rotational mirror is fixed with d = 20 µm, and then the plate is moved along x-axis; (**c**) the plate is fixed, and the mirror rotates.

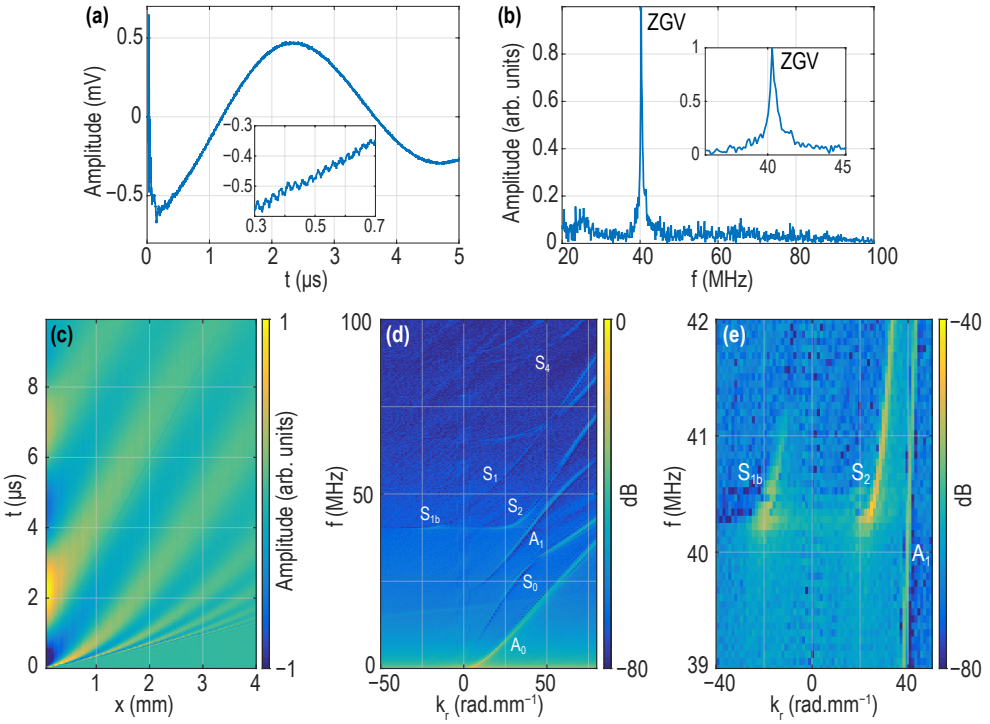

Figure 3. (**a**) A typical measured signal in the aluminum plate and (**b**) its spectra. (**c**) Spatiotemporal measurements (B-scan) obtained in Configuration (2) of the experimental setup (see Figure 2c). (**d**) Wavenumber-frequency diagram obtained by a 2D Fourier Transform of the B-scan shown in (**c**). (**e**) Zoomed-in part of (**d**) around the S_1S_2-ZGV mode.

4. Application of the SLaTCoW Method: Estimation of Ultrasonic Attenuation

The aim of this section is to estimate the ultrasonic attenuation in the polycrystalline aluminum plate using the comparison between experimental and theoretical dispersion curves in the complex plane. To achieve this, the SLaTCoW method [27] is used. This method enables the extraction of complex wave-number information from guided elastic wave measurements. In the SLaTCoW method, unlike the case of the conventional two-dimensional (space and time) Fourier transform [45,46], the time-domain Fourier transform

$$\widetilde{u}(x,\omega) = \int_0^T u(x,t)e^{\imath\omega t}\mathrm{d}t, \tag{3}$$

is associated with a spatial Laplace transform:

$$\overline{u}(s,\omega) = \int_0^L \widetilde{u}(x,\omega)e^{-sx}\mathrm{d}x, \tag{4}$$

where $s = s_r + \imath s_i$ is the complex variable of Laplace. According to Equation (4), it is interesting to note that the quantity $\overline{u}(s,\omega)$ corresponds exactly to the results obtained with a spatial Fourier transform when the real part of s (s_r) is set to zero:

$$\overline{u}[s(s_r = 0, s_i), \omega] = \widetilde{u}(k_r, \omega), \tag{5}$$

therefore implying that the dispersion curves in the real plane could be retrieved from $\overline{u}[s(s_r = 0, s_i], \omega)$. The idea of the SLaTCoW method is to compare the quantity $\overline{u}(s,\omega)$ obtained from the experimental data to a model. Let us assume that the wave field could be written as the sum of the contributions of each of the modes in the frequency domain [27]:

$$\widetilde{u}_{th}(x,\omega) = \sum_n \overline{A}^n e^{ik^n x}\Pi(x - L), \tag{6}$$

where x denotes the spatial coordinate, $\Pi(x-L)$ is the gate function equal to 1 when $x \in [0;L]$ and equal to 0 elsewhere, and $\overline{A}^n$ and k^n are the complex amplitude and complex wavenumber (depending on ω) of the nth mode, respectively. Note that, in our case, the number of modes n is equal to 3, which denotes the three detected Lamb modes: S_{1b}, S_2, and A_1. After applying the Laplace transform to $\widetilde{u}_{th}(x,\omega)$, the theoretical expression $\overline{u}_{th}(s,\omega)$ to which the experimental results is compared takes the following form:

$$\overline{u}_{th}(s,\omega) = \sum_n \overline{A}^n \int_0^L e^{(-s+ik^n)x} dx = L \sum_n \left|\overline{A}^n\right| \frac{\sinh[(-s+ik^n)\frac{L}{2}]}{(-s+ik^n)\frac{L}{2}} e^{i\phi^n + (-s+ik^n)\frac{L}{2}}, \quad (7)$$

where ϕ^n stands for the phase of the complex amplitude $\overline{A}^n$. The recovery of the complex wavenumbers of the three modes is finally performed, frequency by frequency, by minimizing the following cost function:

$$f_{opt}(\omega) = \sqrt{\sum_{s_r} \sum_{s_i} \|\overline{u}(s,\omega) - \overline{u}_{th}(s,\omega)\|^2}. \quad (8)$$

Note that the minimization is performed under constraints with the Nelder–Mead simplex algorithm and the use of the function `fminsearchbnd` in MATLAB. For details and other applications of the SLaTCoW method which are beyond the scope of this manuscript, the readers are referred to the works in [27,47,48].

For the comparison with the experimental results, the complex Lamb wave spectrum is computed applying to elasticity equations a numerical spectral method, as proposed in [49]. The attenuation used to plot the theoretical curves shown in Figure 4 is 0 and 0.4 dB/cm/MHz for the cases without and with accounting for the attenuation, respectively, so that the reader can appreciate the necessity to account for the attenuation in order to retrieve the correct path of the complex branches. The value 0.4 dB/cm/MHz is demonstrated below to be the value allowing the best fit of the theoretical branch of the S_2 mode to the experimental one. Note that the attenuation in the model is supposed to vary linearly with frequency. Although this is a strong assumption, the minimization process presented below is achieved on a small frequency range, i.e., from 40.5 to 41 MHz, where this assumption is acceptable. This small range of frequency is driven by the experimental frequency range in which the S_{1b} mode is observed (see Figure 3e). In Figure 4, the calculated dispersion curves and the results obtained from the measurements and analyzed by the SLaTCoW method are shown. Figure 4a,b shows the dispersion curves in the real (k_r, f) and imaginary (k_i, f) wavenumber–frequency planes for the aluminum plate, respectively. The experimental results for the S_2 mode are depicted by red circles, and those for the S_{1b} mode by blue crosses. The dispersion curves calculated without attenuation are in black dash-dotted and doted lines for the S_2 and S_{1b} modes, respectively. The dispersion curves calculated with attenuation are in red dashed and blue solid lines for the S_2 and S_{1b} modes, respectively. Note that, for the sake of the presentation, the measured curve corresponding to the S_{1b} mode (k_r is negative) in Figure 4a is flipped at the position of the mode S_{-1b} (positive k_r). Note also that, when close to the position of the ZGV point, the signal-to-noise ratio (SNR) decreases due to the attenuation, which explains why there is no experimental points shown in Figure 4 close to the position of the ZGV point.

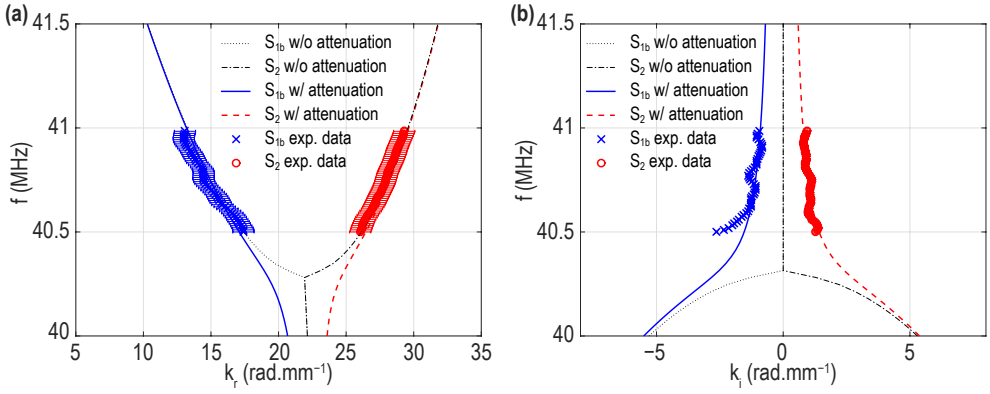

Figure 4. Dispersion curves in (**a**) the plane (k_r, f) and (**b**) the plane (k_i, f). The lines stand for the theoretical dispersion curves with (w/) or without (w/o) taking into account the attenuation. The symbols stands for the experimental data. In (**a**), the error bars of the experimental measurements in the recovery of the real part of the wavenumber is depicted by horizontal segments.

In Figure 4b, it can be noticed that the recovered imaginary parts of the wavenumber for the S_{1b} mode are larger than those recovered for the S_2 mode, which is consistent with the theory showing a slight asymmetry of the S_{1b} and S_2 branches shifting along the k_i-axis. As the frequency decreases towards the ZGV frequency, the experimental S_{1b} branch deviates from the theoretical one, whereas both experimental and theoretical S_2 branches remain coincident. The fact that a deviation from theory of experimental results is seen for the S_{1b} mode and not the S_2 one could be associated to a poorer recovery of the complex wavenumber for the S_{1b} mode due to a lower amplitude of the measured S_{1b} mode, which can be seen in Figure 3e where the S_2 mode has clearly more spectral energy than the S_{1b} mode. Note that the amplitude of the S_{1b} mode being lower than the amplitude of the S_2 mode is actually expected because of the experimental monitoring of the gradients in normal displacement at the surface of the plate, which is theoretically smaller in amplitude for the S_{1b} mode than for the S_2 mode, at least when thermo-elastically excited. We looked at each of the reported data points to check wether the S_{1b} mode complex wavenumber was picked within the noise floor or could be trusted, and we stopped the recovery where we were not confident. Therefore, although a biased recovery may explain the deviation, we are not excluding that other unknown factor(s) participate in it. Nevertheless, the experimental results show good agreement with the theoretical calculations when the attenuation is accounted for. In the real plane, no difference between the case with or without attenuation is noticed. However, the effect of the attenuation (repulsion of the branches) is clearly observed experimentally when the imaginary part of the wavenumber is recovered (see Figure 4b). The error bars of the experimental measurements in the real wavenumber plane (red circle and blue cross in Figure 4a) stand for $2\pi/L$, with $L = 4$ mm the scanning distance along the x-axis.

The extra information given by k_i is useful for assessing the ultrasonic attenuation of the tested sample. To do so, a minimization process, with the attenuation as a parameter and allowing the best fit (least mean square) of the experimental dispersion curves (in the complex plane) to the theoretical dispersion curves accounting for attenuation, is performed. This process is illustrated in Figure 5. The experimental results shown in Figure 4b in the plane (k_i, f) are reported in Figure 5a. The color map shown in Figure 5a stands for the change in the position of the S_2 and S_{1b} branches with changing the ultrasonic attenuation α from 0 (bright yellow) to 1 dB/cm/MHz (dark blue): the larger is the attenuation, the larger is the distance between the two branches in the plane (k_i, f). The minimization process is illustrated in Figure 5b showing, for three cases, the root-mean-square deviation (RMSD) between the measured (k_i^{exp}) and calculated (k_i^{th}) imaginary parts of the wavenumbers as a function of the attenuation α, where RMSD(α) is defined by:

$$\mathrm{RMSD}(\alpha) = \sqrt{\frac{1}{N}\sum_{n=1}^{N}\left|k_i^{exp}(f_n) - k_i^{th}(f_n,\alpha)\right|^2}. \quad (9)$$

In Figure 5b, the red circles, blue crosses, and black triangles represent RMSD(α) in the following three cases, respectively: (i) using only experimental and calculated results of the S_2 mode, the attenuation is then named α_2 and is estimated to be 0.40 ± 0.01 dB/cm/MHz; (ii) using only experimental and calculated results of the S_{1b} mode, the attenuation is then named α_1 and is estimated to be 0.54 ± 0.01 dB/cm/MHz; (iii) using experimental and calculated results of both the S_2 and S_{1b} modes, the attenuation is then named α and is estimated to be 0.47 ± 0.01 dB/cm/MHz. The obtained ultrasonic attenuation values are shown in Table 2 together with those from the literature for aluminum [50]. Note that the proposed precision ± 0.01 comes from the step used in the calculation for the parameter α. It should be mentioned that the attenuation α_1 obtained by using only the results of the S_{1b} mode is larger than α_2 obtained with the S_2 mode, which may be due to a biased complex wavenumber recovery, as discussed above.

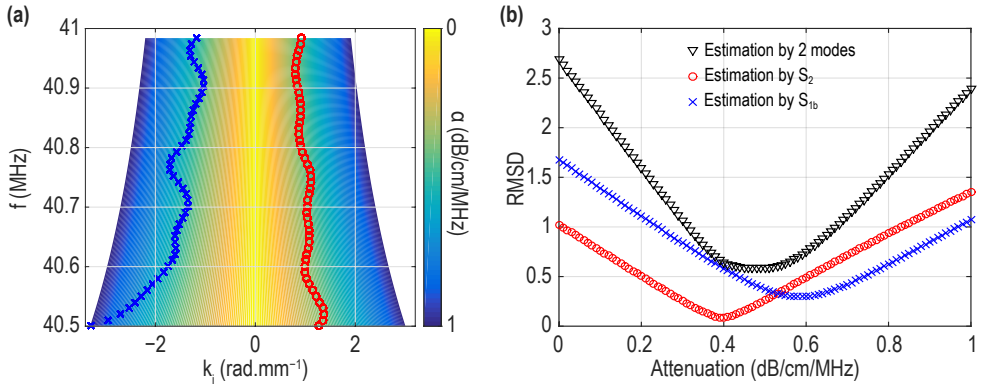

Figure 5. Illustration of the minimization process: (**a**) map in the plane (k_i, f) of the change in the position of the S_2 and S_{1b} theoretical branches with changing the ultrasonic attenuation α from 0 (bright yellow) to 1 dB/cm/MHz (dark blue), the experimental results shown in Figure 4b are reported; (**b**) curves showing the evolution of the root-mean-square deviation (RMSD) vs. α, calculated with the S_2 mode (red circles), the S_{1b} mode (blue crosses), and both the S_2 and S_{1b} modes (black triangles).

As shown in Table 2, the values of the ultrasonic attenuation α estimated in this work are not similar to those measured in the literature [50]. However, the mechanisms for phonon attenuation are not the same. Note that the values of the attenuation α_{lit} (see Table 2) are from [50] (Table III, p. 1053), in which the attenuation is measured along different propagation directions in aluminum. We selected each time the value in the table measured at the closest frequency to our case: 30.7 MHz in the [100] propagation direction, 35.4 MHz in the [110] propagation direction, and 31 MHz in the [111] direction. Several points should be mentioned here that could explain the difference between the values estimated using the proposed method and those reported in the literature:

- The samples used in the literature are single crystals (attenuation is mainly due to coupling to electrons mediated by deformation potential), while the sample used in this work is a polycrystalline plate (attenuation could be due to grain boundary scattering, interaction with dislocations, etc.).
- The purity of the samples used in experiments are not exactly the same. For example, in [50], the purity of aluminum is 99.9999% or 99.999%, but the aluminum sample used in this work is with purity of 99.0%.
- In [50], the authors measured the ultrasonic attenuation along specific and different propagation directions (namely, [100], [110], and [111] of aluminum single crystal), whereas the attenuation obtained in this work is measured in a polycrystalline alu-

minum sample and potentially over multiple grains, which would tend to increase the attenuation.

- The low SNR due to the attenuation, where the estimation is done close to the ZGV point, is the main source of measurement uncertainty in our experiments and could thus be an additional source for the discrepancy.

Although the sample used in this study and those measured in the literature are not the same (as explained in the first point above), the results of ultrasonic attenuation (α) obtained in this work (see Table 2) are still inspiring. Hence, the comparison with α measured by other means on the same tested sample could strengthen the confidence in our results in order to fully demonstrate the quantitative measurement ability of the proposed method. Furthermore, the all-optical technique used in this paper, based on slowly propagating modes in the vicinity of the ZGV point, could also give access to the local mechanical properties and thickness of the sample by using the value of the ZGV resonance frequency. Therefore, the method shows good ability for determining, at the same time, the mechanical properties and the ultrasonic attenuation of samples with plate-like structures.

Table 2. Estimated ultrasonic attenuation in aluminum.

Attenuation	Value (dB/cm/MHz)	
α_2	0.40 ± 0.01	Exp.
α_1	0.54 ± 0.01	Exp.
α	0.47 ± 0.01	Exp.
α_{lit} [100]	0.26 ± 0.04	Ref. [50]
α_{lit} [110]	0.30 ± 0.01	Ref. [50]
α_{lit} [111]	0.230 ± 0.006	Ref. [50]

The local attenuation, namely the ultrasonic attenuation measured at one local point of the scanning distance on the aluminum plate, is estimated by using the approach reported in [24], and the attenuation coefficient (denoted by α_{loc}) is defined by the following formula [24]:

$$\alpha_{loc} = 1/(V_{ph}\tau), \tag{10}$$

where $V_{ph} = \omega/k_{S_1S_2}$ is the phase velocity at the S_1S_2-ZGV point (see Figure 1 in Section 2) and $\tau = 2Q_{Al}/\omega$ is the time-decay constant (see Section 3). At the S_1S_2-ZGV point, we get $V_{ph} = 11.54$ km/s and $\tau = 0.48$ µs. Using the values of V_{ph} and τ in Equation (10), we get $\alpha_{loc} = 15.61$ dB/cm, which is equal to 0.39 dB/cm/MHz if divided by the ZGV resonance frequency at 40.28 MHz. The value of the attenuation coefficient calculated by Equation (10) is lower than, but quite similar to, that estimated by the presented approach in this work (see Table 2). The difference between the values of the attenuation coefficients calculated by the two different methods can be mainly explained by the following two reasons. First, the method in [24] provides the local attenuation at the position of a point on the sample, while the method proposed in this work provides the global attenuation over a given distance on the sample, here 4 mm. The value of α (estimated by the proposed method) can be then considered as the average of α_{loc} (estimated by the method in [24]) measured at each local point along the given distance on the sample. Second, the value of α is estimated over the range of frequency ($f \in [40.5, 41.0]$ MHz) and that of α_{loc} is estimated at the ZGV resonance frequency ($f_{S_1S_2} = 40.28$ MHz).

Before the conclusion of this work, we propose hereby another application of the SLaT-CoW method for future work: the monitoring of cumulative damage [20,21] in materials through the estimation of the ultrasonic attenuation from experimental measurements done at different stages of the fatigue process. Indeed, when the material fatigues, an increase in the ultrasonic attenuation is expected. Its monitoring should hence be insightful and could give information about the fatigue progress and stage. Recently, in [21], we observed the dramatic drop of the experimental quality factor in the early fatigue stage in aluminum,

compared to the numerically calculated values by a theoretical modeling considering only a thickness variation of the fatigued plate, which required the improvement of the conducted modeling by accounting for the change of material attenuation. The proposed method can thus be used for a better understanding of ultrasonic attenuation at different fatigue stages through its global estimation along the damaged region, which could help improving/completing the empirically based theoretical modeling proposed in [21].

5. Conclusions

We present in this paper the application of the SLaTCoW method to the ZGV Lamb modes in order to extract the ultrasonic attenuation of a thin plate of polycrystalline aluminum. With the spatial Laplace transform, the dispersion curves in the complex wavenumber plane can be reconstructed and used for extracting the ultrasonic attenuation. With the same set of measurements, it is also possible to measure the mechanical properties and thickness of the tested plate, making the proposed method a handy and versatile tool for material characterization. The experimental results are positively compared with values reported in the literature, which were measured by other means. From the comparison between experimental measurements and theoretical calculations, a good agreement between them is found and shows the ability of this proposed method for estimating the ultrasonic attenuation in polycrystalline aluminum. Another method, based on the time-decay law of ZGV resonance, as presented in [24], is applied to the same experimental measurements, in order to extract the value of the local attenuation of the sample and then be compared with the values estimated by the proposed method in this work. The difference between the estimated results using two different methods has been found and discussed. It has also been proposed that this method can be very useful in non-destructive evaluation. For example, it could allow the extraction of the evolution of the ultrasonic attenuation in cumulatively damaged plate structures [20,21]. Therefore, one of the research focuses in the future could be the comparison of the ultrasonic attenuation obtained by this means between intact and damaged (bending, tensile testing, three points testing, etc.) specimens for better understanding of the nature of specific type of damages in metallic materials and alloys.

Author Contributions: G.Y., S.R., N.C., V.E.G. and V.T. conceived and designed the experiments; A.G., A.D. and J.-P.G. conceived and contributed to the analysis method; G.Y. and S.R. performed the experiments; G.Y., S.R. and J.-P.G. analyzed the data; G.Y. prepared the original draft; G.Y., S.R., J.-P.G., A.D., A.G., N.C., V.E.G. and V.T. reviewed the manuscript. All authors have read and agreed to the published version of the manuscript.

Funding: This research received no external funding.

Institutional Review Board Statement: Not applicable.

Informed Consent Statement: Not applicable.

Data Availability Statement: The data presented in this study are available from the corresponding author upon reasonable request.

Conflicts of Interest: The authors declare no conflict of interest.

References

1. Toozandehjani, M.; Matori, K.A.; Ostovan, F.; Mustapha, F.; Zahari, N.I.; Oskoueian, A. On the correlation between microstructural evolution and ultrasonic properties: A review. *J. Mat. Sci.* **2015**, *50*, 2643–2665. [CrossRef]
2. Bhatia, A. *Ultrasonic Absorption: An Introduction to the Theory of Sound Absorption and Dispersion in Gases, Liquids, and Solids*; Dover Publications: Mineola, NY, USA, 1985.
3. Schmerr, L.W., Jr. *Fundamentals of Ultrasonic Nondestructive Evaluation: A Modeling Approach*, 2nd ed.; Springer Series in Measurement Science and Technology; Springer International Publishing: Cham, Switzerland, 2016.
4. Hutchins, D.A.; Lundgren, K.; Palmer, S.B. A laser study of transient Lamb waves in thin materials. *J. Acoust. Soc. Am.* **1989**, *85*, 1441–1448. [CrossRef]
5. Scandrett, C.; Vasudevan, N. The propagation of time harmonic Rayleigh-Lamb waves in a bimaterial plate. *J. Acoust. Soc. Am.* **1991**, *89*, 1606–1614. [CrossRef]

6. Minonzio, J.G.; Talmant, M.; Laugier, P. Guided wave phase velocity measurement using multi-emitter and multi-receiver arrays in the axial transmission configuration. *J. Acoust. Soc. Am.* **2010**, *127*, 2913–2919. [CrossRef] [PubMed]
7. Mezil, S.; Bruno, F.; Raetz, S.; Laurent, J.; Royer, D.; Prada, C. Investigation of interfacial stiffnesses of a tri-layer using Zero-Group Velocity Lamb modes. *J. Acoust. Soc. Am.* **2015**, *138*, 3202–3209. [CrossRef] [PubMed]
8. Bjurström, H.; Ryden, N. Detecting the thickness mode frequency in a concrete plate using backward wave propagation. *J. Acoust. Soc. Am.* **2016**, *139*, 649–657. [CrossRef]
9. Prada, C.; Balogun, O.; Murray, T.W. Laser-based ultrasonic generation and detection of zero-group velocity Lamb waves in thin plates. *Appl. Phys. Lett.* **2005**, *87*, 194109. [CrossRef]
10. Gibson, A.; Popovics, J. Lamb Wave Basis for Impact-Echo Method Analysis. *J. Eng. Mech.* **2005**, *131*, 438–443. [CrossRef]
11. Clorennec, D.; Prada, C.; Royer, D.; Murray, T.W. Laser impulse generation and interferometer detection of zero group velocity Lamb mode resonance. *Appl. Phys. Lett.* **2006**, *89*, 024101. [CrossRef]
12. Clorennec, D.; Prada, C.; Royer, D. Laser ultrasonic inspection of plates using zero-group velocity lamb modes. *IEEE Trans. Ultrason. Ferroelectr. Freq. Control* **2010**, *57*, 1125–1132. [CrossRef]
13. Cès, M.; Clorennec, D.; Royer, D.; Prada, C. Thin layer thickness measurements by zero group velocity Lamb mode resonances. *Rev. Sci. Instrum.* **2011**, *82*, 114902. [CrossRef] [PubMed]
14. Clorennec, D.; Prada, C.; Royer, D. Local and noncontact measurements of bulk acoustic wave velocities in thin isotropic plates and shells using zero group velocity Lamb modes. *J. Appl. Phys.* **2007**, *101*, 034908. [CrossRef]
15. Prada, C.; Clorennec, D.; Royer, D. Local vibration of an elastic plate and zero-group velocity Lamb modes. *J. Acoust. Soc. Am.* **2008**, *124*, 203–212. [CrossRef]
16. Laurent, J.; Royer, D.; Prada, C. Temporal behavior of laser induced elastic plate resonances. *Wave Motion* **2014**, *51*, 1011–1020. [CrossRef]
17. Raetz, S.; Laurent, J.; Dehoux, T.; Royer, D.; Audoin, B.; Prada, C. Effect of refracted light distribution on the photoelastic generation of zero-group velocity Lamb modes in optically low-absorbing plates. *J. Acoust. Soc. Am.* **2015**, *138*, 3522–3530. [CrossRef]
18. Prada, C.; Clorennec, D.; Murray, T.W.; Royer, D. Influence of the anisotropy on zero-group velocity Lamb modes. *J. Acoust. Soc. Am.* **2009**, *126*, 620–625. [CrossRef]
19. Faëse, F.; Raetz, S.; Chigarev, N.; Mechri, C.; Blondeau, J.; Campagne, B.; Gusev, V.E.; Tournat, V. Beam shaping to enhance zero group velocity Lamb mode generation in a composite plate and nondestructive testing application. *NDT E Int.* **2017**, *85*, 13–19. [CrossRef]
20. Yan, G.; Raetz, S.; Chigarev, N.; Gusev, V.E.; Tournat, V. Characterization of Progressive Fatigue Damage in Solid Plates by Laser Ultrasonic Monitoring of Zero-Group-Velocity Lamb Modes. *Phys. Rev. Appl.* **2018**, *9*, 061001. [CrossRef]
21. Yan, G.; Raetz, S.; Chigarev, N.; Blondeau, J.; Gusev, V.E.; Tournat, V. Cumulative fatigue damage in thin aluminum films evaluated non-destructively with lasers via zero-group-velocity Lamb modes. *NDT E Int.* **2020**, *116*, 102323. [CrossRef]
22. Balogun, O.; Cole, G.; Huber, R.; Chinn, D.; Murray, T.; Spicer, J. High-spatial-resolution sub-surface imaging using a laser-based acoustic microscopy technique. *IEEE Trans. Ultrason. Ferroelectr. Freq. Control* **2011**, *58*, 226–233. [CrossRef] [PubMed]
23. Xie, Q.; Mezil, S.; Otsuka, P.H.; Tomoda, M.; Laurent, J.; Matsuda, O.; Shen, Z.; Wright, O.B. Imaging gigahertz zero-group-velocity Lamb waves. *Nat. Commun.* **2019**, *10*, 2228. [CrossRef] [PubMed]
24. Prada, C.; Clorennec, D.; Royer, D. Power law decay of zero group velocity Lamb modes. *Wave Motion* **2008**, *45*, 723–728. [CrossRef]
25. Berer, T.; Grünsteidl, C.; Rothemund, R.; Kreuzer, S.; Ryzy, M.; Hettich, M.; Veres, I.A. Determination of longitudinal and transversal attenuation coefficients in the frequency domain using zero group velocity Lamb waves. In Proceedings of the 2019 IEEE International Ultrasonics Symposium (IUS), Glasgow, Scotland, 6–9 October 2019; pp. 1974–1976. [CrossRef]
26. Hodé, R.; Raetz, S.; Blondeau, J.; Chigarev, N.; Cuvillier, N.; Tournat, V.; Ducousso, M. Nondestructive evaluation of structural adhesive bonding using the attenuation of zero-group-velocity Lamb modes. *Appl. Phys. Lett.* **2020**, *116*, 104101. [CrossRef]
27. Geslain, A.; Raetz, S.; Hiraiwa, M.; Abi Ghanem, M.; Wallen, S.P.; Khanolkar, A.; Boechler, N.; Laurent, J.; Prada, C.; Duclos, A.; et al. Spatial Laplace transform for complex wavenumber recovery and its application to the analysis of attenuation in acoustic systems. *J. Appl. Phys.* **2016**, *120*, 135107. [CrossRef]
28. Solie, L.P.; Auld, B.A. Elastic waves in free anisotropic plates. *J. Acoust. Soc. Am.* **1973**, *54*, 50–65. [CrossRef]
29. Prosser, W.H.; Seale, M.D.; Smith, B.T. Time-frequency analysis of the dispersion of Lamb modes. *J. Acoust. Soc. Am.* **1999**, *105*, 2669–2676. [CrossRef]
30. Niethammer, M.; Jacobs, L.J.; Qu, J.; Jarzynski, J. Time-frequency representations of Lamb waves. *J. Acoust. Soc. Am.* **2001**, *109*, 1841–1847. [CrossRef]
31. Simonetti, F.; Lowe, M.J.S. On the meaning of Lamb mode nonpropagating branches. *J. Acoust. Soc. Am.* **2005**, *118*, 186–192. [CrossRef]
32. Xu, K.; Ta, D.; Moilanen, P.; Wang, W. Mode separation of Lamb waves based on dispersion compensation method. *J. Acoust. Soc. Am.* **2012**, *131*, 2714–2722. [CrossRef]
33. Kausel, E. Number and location of zero-group-velocity modes. *J. Acoust. Soc. Am.* **2012**, *131*, 3601–3610. [CrossRef]
34. Hussain, T.; Ahmad, F. Lamb modes with multiple zero-group velocity points in an orthotropic plate. *J. Acoust. Soc. Am.* **2012**, *132*, 641–645. [CrossRef] [PubMed]

35. Every, A.G. Intersections of the Lamb mode dispersion curves of free isotropic plates. *J. Acoust. Soc. Am.* **2016**, *139*, 1793–1798. [CrossRef]
36. Auld, B. *Acoustic Fields and Waves in Solids*; R. E. Krierger Publishing Compagny: Malabar, FL, USA, 1990; Volume II.
37. Royer, D.; Dieulesaint, E. *Elastic Waves in Solids I: Free and Guided Propagation*; Springer: Berlin/Heidelberg, Germany, 2000.
38. Biot, M.A. General Theorems on the Equivalence of Group Velocity and Energy Transport. *Phys. Rev.* **1957**, *105*, 1129–1137. [CrossRef]
39. Olmstead, M.A.; Amer, N.M.; Kohn, S.; Fournier, D.; Boccara, A.C. Photothermal displacement spectroscopy: An optical probe for solids and surfaces. *Appl. Phys. A* **1983**, *32*, 141–154. [CrossRef]
40. Rothenberg, J.E. Observation of the transient expansion of heated surfaces by picosecond photothermal deflection spectroscopy. *Opt. Lett.* **1988**, *13*, 713–715. [CrossRef] [PubMed]
41. Royer, D.; Dieulesaint, E. *Elastic Waves in Solids II: Generation, Acousto-Optic Interaction, Applications*; Springer: Berlin/Heidelberg, Germany, 2000.
42. Putman, C.A.J.; De Grooth, B.G.; Van Hulst, N.F.; Greve, J. A detailed analysis of the optical beam deflection technique for use in atomic force microscopy. *J. Appl. Phys.* **1992**, *72*, 6–12. [CrossRef]
43. Mezil, S.; Chigarev, N.; Tournat, V.; Gusev, V. All-optical probing of the nonlinear acoustics of a crack. *Opt. Lett.* **2011**, *36*, 3449–3451. [CrossRef]
44. Higuet, J.; Valier-Brasier, T.; Dehoux, T.; Audoin, B. Beam distortion detection and deflectometry measurements of gigahertz surface acoustic waves. *Rev. Sci. Instrum.* **2011**, *82*, 114905. [CrossRef]
45. Alleyne, D.; Cawley, P. A two-dimensional Fourier transform method for the measurement of propagating multimode signals. *J. Acoust. Soc. Am.* **1991**, *89*, 1159–1168. [CrossRef]
46. Gao, W.; Glorieux, C.; Thoen, J. Laser ultrasonic study of Lamb waves: Determination of the thickness and velocities of a thin plate. *Int. J. Eng. Sci.* **2003**, *41*, 219–228. [CrossRef]
47. Schwan, L.; Geslain, A.; Romero-García, V.; Groby, J.P. Complex dispersion relation of surface acoustic waves at a lossy metasurface. *Appl. Phys. Lett.* **2017**, *110*, 051902. [CrossRef]
48. Cebrecos, A.; Romero-García, V.; Groby, J.P. Complex Dispersion Relation Recovery from 2D Periodic Resonant Systems of Finite Size. *Appl. Sci.* **2019**, *9*, 478. [CrossRef]
49. Pagneux, V.; Maurel, A. Determination of Lamb mode eigenvalues. *J. Acoust. Soc. Am.* **2001**, *110*, 1307–1314. [CrossRef] [PubMed]
50. Hepfer, K.C.; Rayne, J.A. Ultrasonic Attenuation in Aluminum. *Phys. Rev. B* **1971**, *4*, 1050–1064. [CrossRef]